Supplemental Information

Structures of The HIN Domain:DNA Complexes Reveal Ligand Binding and Activation Mechanisms of The AIM2 Inflammasome and IFI16 Receptor

Tengchuan Jin, Andrew Perry, Jiansheng Jiang, Patrick Smith, James A. Curry, Leonie Unterholzner, Zhaozhao Jiang, Gabor Horvath, Vijay Rathinam, Ricky W. Johnstone, Veit Hornung, Eicke Latz, Andrew G. Bowie, Katherine A. Fitzgerald, and T. Sam Xiao

An inventory of all supplemental items

SUPPLEMENTAL TEXT

The Antimicrobial Peptide LL-37 Competes with The AIM2 HIN Domain for DNA-Binding

LL-37 is a highly positively charged antimicrobial peptide that disrupts microbial membrane and activates cell surface receptors (Yang et al., 2001; Tokumaru et al., 2005). Recently, it was found to alleviate skin inflammation in

psoriasis lesions by sequestration of cytosolic DNA and suppression of IL-1β release, perhaps acting through inhibition of AIM2 signaling (Dombrowski et al., 2011). The positive charge of LL-37 was essential for this inhibition, and a shorter form of this peptide KS-30 retains the same activity. This was the first report of the anti-inflammatory activity of LL-37 relevant to inflammasome suppression, although direct inhibition of AIM2 by LL-37 was not demonstrated. To understand the mechanism of the AIM2 signaling modulation by LL-37/KS-30, we performed DNA binding assays with the AIM2 HIN domain and KS-30. We show that KS-30 inhibited the AIM2 HIN:DNA interaction (Figure S5F), and it bound DNA with an apparent Kd of 0.17 μM (Figures S4A). This is in contrast to the inhibition of the HIN:DNA binding by the AIM2 PYD domain, which did not bind DNA but instead may obstruct the DNA-binding surface at the HIN domain. We also demonstrated that the scrambled version of the KS-30 peptide failed to inhibit the HIN:DNA interaction (Figure S5F), suggesting that the helical structure of the peptide as well as its basic charge are likely required for its ability to suppress AIM2 signaling. Although there is currently no structural characterization of LL-37 in complex with DNA, we note that a major part of the DNA-binding surface from the AIM2 HIN domain are Lysines and Arginines at the OB1-OB2 linker (see Results in the main text) that adopts α helical conformation, which is similar to the structure of the isolated LL-37 (2K6O) (Wang, 2008).

Binding of dsDNA versus ssDNA by The OB Folds

Previously the OB fold was shown to bind ssDNA, as in the crystal structure of the single-stranded-DNA-binding (SSB) domain for one of the trimeric subunits (RPA70) of the replication protein A (RPA) (Bochkarev et al., 1997). Comparison of the RPA:ssDNA and HIN:dsDNA structures demonstrates that the OB folds employ different binding surface for ssDNA or dsDNA (Figures 3C and S5G-I). The RPA SSB uses its long β1'-β2 loops from OB1 and OB2 to form a ssDNA binding cleft, which is absent in the HIN domains. In contrast, the positively charged linker helices at the dsDNA binding site of the HIN domains are absent in the RPA SSB, which instead contains a highly acidic surface near its short linker (Figure S5H). Superposition of the OB1 modules from both AIM2 HIN and RPA SSB domains also illustrates a large domain rotation for the OB2 folds, such that the OB2 of RPA SSB would clash with the dsDNA bound to the AIM2 HIN domain (Figure S5I). It is clear that unique structural characteristics of the OB-fold proteins dictate their binding preference for ss or dsDNA.

We were also able to co-crystallize IFI16 HINb in complex with an ssDNA ODN 393, and the structure and packing of the IFI16 HINb domains are identical to the IFI16 HINb-dsDNA crystals (Figure S2G). Although we were not able to formally confirm the presence of the ssDNA in the crystals, we did notice that IFI16 HINb itself (without DNA) was crystallized in completely different crystal forms (Liao et al., 2011). Unfortunately, no electron density for the ssDNA was visible in the crystal lattice at 1.8 Å resolution, perhaps partly due to weak binding or multiple conformations adopted by the ssDNA in the crystal.

SUPPLEMENTAL EXPERIMENTAL PROCEDURES

Protein Expression and Purification

The protein sequences of human AIM2 (NCBI accession # NP_004824) and human IFI16 (Q16666) were referred to in this study. The AIM2 HIN (residues 144-343) and IFI16 HINb (residues 571-766) domains were cloned into a pET30a vector with a TEV cleavable N-terminal protein G β1 domain (GB1) tag. The GB1 coding plasmid was a gift from Dr. Gerhard Wagner at Harvard Medical School. The TEV coding plasmid was a gift from Dr. David Waugh at the National Cancer Institute. Transformed BL21 (DE3) Codon Plus RIPL cells (Stratagene, Santa Clara, CA) were grown at 37 °C until OD600 reached 1.2. Cells were then induced with 0.2 mM IPTG at 18 °C for 4 hours, harvested and resuspended in buffer A (20 mM Tris-HCl, pH 8.0, 100 mM NaCl) plus 5 mM imidazole and supplemented with DNase (Biomatik, Wilmington, DE) and protease inhibitors (Roche Applied Science, Indianapolis, IN). Cells were lysed by sonication, and soluble protein was purified from cell lysate by Hisprep IMAC column (GE Healthcare Bio-Sciences, Piscataway, NJ). Non-specific nucleic acid contaminants were removed by polyethyleneimine (PEI) precipitation at a final concentration of 0.1% followed by ammonium sulfate precipitation to a final concentration of 3M. The protein pellet was dissolved in buffer A before TEV protease cleavage. Further purification was carried out with a second IMAC column and size exclusion chromatography. The AIM2 HIN domain was also expressed using a His6-tag plus an MBP fusion tag at the N-terminus to improve

the yield of the purified samples. The purification protocol was the same as outlined above. The wild type or mutant PYD domain (residues 1-107) of AIM2 was cloned into the same His6-MBP tagged expression vector. The mutant PYD domain contains mutations of E7A, L11A, D15A, D19A and E20A, residues located at the HIN:PYD interface based on the docking results (see the modeling methods below). The PYD domains were purified using the same protocol as outlined above, without the PEI and ammonium sulfate precipitation steps.

Crystallization

DNA oligos were synthesized by IDT (Coralville, IA) without 5'-phosphate. Oligos were dissolved in buffer B (20 mM Hepes-Na, pH 7.4, 100 mM KCl and 5 mM DTT). Oligo pairs were mixed at 1:1 molar ratio, heated to 95 °C, and annealed by slow cooling to room temperature. Annealed dsDNA were added to protein solutions in buffer B and concentrated by centrifugal concentrators (Millipore, Billerica, MA) to 10-20 mg/ml before setting up hanging drop vapor diffusion method for crystallization.

Two dsDNA were used for crystallization with the AIM2 HIN domain (Tables S1 and S2): a palindromic 20mer self-annealed from ODN 786 (crystal form I), and a 19mer dsDNA annealed from ODN 736 and ODN 737 (crystal form II). The AIM2 HIN:DNA complexes were crystallized with a well solution containing 8% PEG 1000, 100 mM KCl, 10 mM $MgCl_2$, and 100 mM Mes-Na, pH 6.5. To prepare the IFI16 HINb-dsDNA complex, ODN 723 and ODN 724 (IFI 16

crystal form I) were annealed to form a dsDNA and mixed with IFI16 HINb and concentrated. The complex was crystallized with a reservoir solution containing 20% PEG 3350, 100 mM potassium formate, and 100 mM Hepes-Na, 7.0. A single stranded 8mer DNA ODN 393 (crystal form II) was also used to co-crystallize with IFI16 HINb with a reservoir solution containing 20% PEG 1500, 10 mM $MgCl_2$, and 100 mM Mes-Na, pH 6.0. An IFI16 HINb mutant containing mutations of K663A and R667A was crystallized in the presence of a 28mer dsDNA annealed from ODN 758 and ODB 759 (crystal form III). The reservoir solution contained 20% PEG 3350 and 200 mM KCl. 20% ethylene glycol (v/v) was added to the reservoir solutions as the cryoprotectant to freeze the AIM2 HIN or IFI16 HINb crystals in liquid nitrogen for X-ray diffraction data collection.

X-ray Diffraction, Structure Determination and Refinement

X-ray diffraction data were collected at GM/CA-CAT at the Advanced Photon Source, Argonne National Laboratory (ANL). Data were processed with HKL2000 program suite (Zbyszek Otwinowski, 1997) and XDS (Kabsch, 2010). The IFI16 HINb-DNA and AIM2 HIN:DNA structures were determined by molecular replacement (MR) with Phaser (McCoy et al., 2007) from the CCP4 program suite (Potterton et al., 2003). A deposited IFI16 HINb structure (3B6Y) (Liao et al., 2011), and ideal dsDNA from Coot (Emsley and Cowtan, 2004) and make_na server (Lakshiminarayanan and Sasisekharan, 1970) were used as the initial search models. Electron density maps calculated with phases from the MR

solutions clearly showed positive densities for the dsDNA sugar-phosphate backbones (Figure S1), and were consistent with molecular replacement solutions using B-DNA but not A- or Z-DNA search models, as the diameters of the latter two forms are either too big or too small for the space among the HIN domains. We tested dsDNA of different lengths (8-mer to 70-mer) for crystallization, and found out that only ~16-mer or ~20mer dsDNA can be accommodated by the crystallographic symmetry of the IFI16 HINb or AIM2 HIN crystals, respectively, such that unambiguous electron densities would allow for building of the dsDNA structures. In reality, and similar to the crystal structure of TLR3 in complex with dsRNA (Liu et al., 2008), the dsDNA could flip its direction and/or slide along the sugar-phosphate backbone in the crystal lattice.

Structure building and refinement were carried out with Coot (Emsley and Cowtan, 2004) and Phenix (Adams et al., 2010). DNA base pair hydrogen bonding restraints from the PDBto3D restraints server (Laurberg et al., 2008) and TLS parameters generated by the TLSMD server (Painter and Merritt, 2006) or Phenix (Adams et al., 2010) were applied throughout the refinement. Twinned refinement protocols were applied for the AIM2 crystal forms I and II and IFI16 crystal form I as suggested by program Xtriage from Phenix (Adams et al., 2010). Analysis of the diffraction dataset for the AIM2 crystal form I showed that it has an estimated twinning fraction of 0.27 (Britton analysis) or 0.23 (H-test) with a twin operator of (h, -k, -l). Analysis using program TRUNCATE from the CCP4 suite (Lee and Richards, 1971; Potterton et al., 2003) also confirmed the presence of twinning. Similarly, the AIM2 crystal form II dataset has an estimated

twinning fraction of 0.43 (Britton analysis) or 0.45 (H-test) with a twin operator of (h, -k, -l). Analysis of the dataset for the IFI16 form I indicated that it has an estimated twinning fraction of 0.45 (Britton analysis) or 0.48 (H-test), with a twin operator of (h, -h-k, -l). The above twin operators were incorporated in the Phenix refinement protocols for the respective structures. The twinned refinement protocol resulted in decreased R and R free factors, confirming the diagnosis of twinning.

The final refined models exhibit no gross structural changes for the IFI16 HINb upon DNA binding, and the refined dsDNA structures remain the B-form configuration with characteristic χ and δ torsion angles, per analysis with program 3DNA (Lu and Olson, 2008). The crystal structures were validated by the Molprobity server (Chen et al., 2010) and RCSB ADIT validation server (Yang et al., 2004). Solvent accessible surface area was calculated with program Areaimol from the CCP4 suite (Lee and Richards, 1971; Potterton et al., 2003). Electrostatics surfaces were calculated with program Delphi (Honig and Nicholls, 1995) and displayed with program Pymol (Delano Scientific LLC, San Carlos, CA).

Fluorescence Polarization (FP) Assay

5’-Fluorescein (FAM) labeled (IDT, Coralville, IA) 20mer DNA oligo ODN 787 (Table S1) was dissolved in buffer A and annealed with its reverse complement ODN 788 by heating to 95 °C and slowly cooling to room

temperature. 3 nM dsDNA were used for the AIM2 HIN and IFI16 HINb FP assays. Purified IFI16 HINb or AIM2 HIN samples were mixed with the FAM labeled dsDNA and diluted into assay buffers containing 20 mM Hepes-Na, pH 7.4 and various concentrations of NaCl (see below). The mixtures were then aliquoted in triplets into black 96 well plates and fluorescence polarization was measured with a Paradigm spectrometer (Molecular Devices, Sunnyvale, CA). The AIM2 HIN domains were measured in a buffer containing 100 mM NaCl, and the IFI16 HINb domains with 50 mM NaCl due to their lower affinities for DNA. MBP fusion proteins were used in most FP assays for the AIM2 HIN domain and the fusion tag had minimal impact on the HIN:DNA binding (Figure S4B). To test the effects of salt concentrations on DNA binding, 50 mM, 100 mM, 200 mM, 300 mM and 400 mM NaCl were used for the AIM2 HIN domain, and 20 mM, 50 mM, 100 mM and 200 mM NaCl were used for the IFI16 HINb domain. For the inhibition assay, 0.1 μM MBP-AIM2 HIN domain was pre-incubated with 3 nM FAM-labeled 20mer dsDNA probe, and increasing concentrations of the wild type and mutant AIM2 PYD domain, or the KS-30 peptide and its scrambled version, were added to the mixture and the fluorescence polarization was measured. Data were analyzed and plotted using program GraphPad Prism version 5.0, GraphPad Software, San Diego, CA.

Confocal Microscopy

Co-localization of the AIM2 HIN domains with DNA was studied with HEK293T cells and immortalized AIM2 deficient macrophages. HEK293T cells were grown on glass coverslips and transfected with 2µg/ml wild type or the m12 mutant HA-AIM2-HIN constructs using calcium phosphate. 24 hours after transfection, cells were fixed with 4% paraformaldehyde in phosphate-buffered saline (PBS), permeabilized with 0.5% Triton in PBS, pre-incubated for 1 hour in blocking buffer (5% BSA and 0.05% Tween-20 in PBS), and stained for 3 hours with anti-HA antibody (Alexa647 red, Invitrogen, Carlsbad, CA) diluted 1:300 in the blocking buffer. Coverslips were mounted in MOWIOL 4-88 (Calbiochem, Nottingham, UK) containing DAPI (4,6-diamidino-2-phenylindole, blue) at 1 µg/ml. Images were taken on an Olympus FV1000 scanning confocal microscope.

AIM2 deficient macrophages (Rathinam et al., 2010) were immortalized using J2 retrovirus as described (Hornung et al., 2008) and transduced with retroviruses encoding fluorescent (mCerulean, green) wild type or the m12 mutant AIM2 HIN domains and positive cells were selected using puromycin. Cells were plated on CELLview dish (627871, Greiner Bio-One GmbH, Germany) overnight and transfected with a FITC-labeled dsDNA. Live cells were imaged 3 hours after transfection with a Leica SP5 AOBS SMD confocal microscope with a 63x/1.2 water-immersion objective. mCerulean was excited at 458 nm and detected at 463-485 nm (green), and FITC was excited with at 496 nm and detected at 521-589 nm (red). Two five by five mosaic images were obtained at

1200x1200 pixels with 8 vertical slices. For image analysis, the vertical slices were compressed in the Z-axis with maximum intensity projection, and Volocity (PerkinElmer, Inc., MA) was used for identifying specks representing FITC-labeled dsDNA. The ratio of the number of the dsDNA specks that colocalized with the AIM2 HIN domain to the total number of dsDNA specks was determined after setting a threshold on the fluorescence intensity of the AIM2 HIN mCerulean based on the average intensity of the cells.

Reconstitution of The AIM2 Inflammasomes

Reconstitution of the AIM2 inflammasome was carried out as previously described (Hornung et al., 2009). Briefly, HEK293T cells seeded in 96-well plates (2×10^4 cells/well) were transfected with increasing amounts (0, 5, 10, and 40 ng) of HA-tagged hAIM2 full-length expression constructs and Guassia-luciferase-FLAG tagged pro-IL-1β (~54 kDa), procaspase-1 and 0 or 20 ng ASC constructs. After 24 hours, cells were lysed with 1x SDS buffer. The lysates were run on 10% polyacrylamide gels, transferred onto nitrocellulose membrane and probed with mouse anti-IL-1β monoclonal antibody (clone 3ZD, National Cancer Institute, NIH). The expression levels for the hAIM2 proteins were probed with anti-HA antibody (Roche Applied Science, Indianapolis, IN) and anti-AIM2 antibody from R. Johnstone (University of Melbourne, Australia).

Luciferase Reporter Gene Assay

IFN-β-promoter luciferase was a gift from T. Taniguchi (University of Tokyo, Japan). GL3-Renilla vector was made by replacing the firefly luciferase ORF from pGL3-control (Promega, Madison, WI) with the renilla luciferase ORF from pRL-TK (Promega, Madison, WI). STING and IFI16 cDNA were amplified from I.M.A.G.E. clones, and cloned into pCMV-HA or pCMV-myc (Clontech, Mountain View, CA). HEK293T cells were grown in Dulbecco's Modified Eagle's Medium supplemented with 10% fetal bovine serum (Biosera, Ringmer, UK) and 10 µg/ml ciprofloxacin (Sigma, St Louis, MO). Luciferase reporter gene assays were performed with HEK293T cells seeded in 96-well pates and transfected with 0.8 µl Genejuice (Merck Chemicals, Nottingham, UK) per well. 60 ng firefly reporter construct under the control of the IFN-β promoter, and 20 ng GL3-Renilla control plasmid, 5ng STING expression vector and 50 or 150 ng IFI16 expression vector or empty vector were transfected as indicated. 48 hours after transfection, cells were lysed in Passive Lysis Buffer (Promega, Madison, WI), and firefly luciferase activity was measured and normalized to the renilla luciferase activity. Experiments were performed in triplicate and results are shown as mean values with standard deviations. The expression levels of the wild type or mutant full-length IFI16 were measured by immunoblotting with anti-HA antibody (Sigma, St. Louis, MO) 48 hours after transfection.

Stimulation of IL-1β Secretion with dsDNA

Human peripheral blood mononuclear cells (PBMCs) were obtained from healthy, volunteer blood donors under signed informed consent with approval from the Institutional Review Board of the University of Massachusetts Medical School. The PBMCs were isolated from whole human blood by Ficoll-Hypaque density gradient centrifugation. 400,000 PBMCs were cultured in 96-well plates in complete RPMI medium with 10% fetal calf serum. Isolated human PBMCs were primed with LPS (200 pg/ml) for 3 hours and subsequently transfected with the indicated nucleic acids (Table S1) using 200 ng per transfection plus 0.5 µl Lipofectamine 2000 (Invitrogen, Carlsbad, CA). Prior to transfection, oligonucleotides were heated up at 95°C and then slowly cooled down to anneal the DNA. ATP (5 mM) or monosodium urate (MSU, 250 µg/ml) was used as positive controls. Six hours after stimulation supernatants were collected and assayed for IL-1β using ELISA. Data from one representative experiment out of two independent experiments (mean values + SEM) are depicted. LPS, poly(dA:dT) and MSU were obtained from Sigma (St Louis, MO).

Modeling of The AIM2 Inflammasome

Construction of a hypothetical AIM2 inflammasome model was accomplished through sequential docking of the AIM2 PYD model and then the full-length ASC structure onto the HIN:DNA structures from the AIM2 crystal form II. This DNA:AIM2:ASC model with a dsDNA footprint of ~16 bp was then

propagated along a dsDNA staircase five times. The spacing among these five copies were chosen so they are well separated without steric clashes, but was otherwise arbitrary. The total footprint of the AIM2:ASC complexes at the dsDNA is ~100 bp. At present we can not formally exclude the possibility of other forms of oligomerization for the AIM2 inflammasomes.

The AIM2 PYD domain was modeled based on the ASC PYD domain (PDB code 2KN6) (de Alba, 2009) using the MMM server (Rai and Fiser, 2006) (http://manaslu.aecom.yu.edu/MMM/). Docking of the AIM2 PYD domain model onto the AIM2 HIN domain or the AIM2 HIN:DNA complex, and docking of the ASC structure (2KN6) (de Alba, 2009) onto the AIM2:DNA structure was accomplished with program HEX (Ritchie et al., 2008). The resulting model was subjected to energy minimization using the relax mode of the Rosetta program (v3.2) (Kuhlman et al., 2003).

Table S1. List of DNA Oligos and Peptides Used in This Study

DNA Oligos		
	Sequence (5'-3')	**Notes**
ODN 315/316*	CCGCCAGCCCGCGGGCTGGC	FP assay (90% GC)
ODN 317/318*	ATTTAATAATAATTTATTAT	FP assay (0% GC)
ODN 319/320*	GATGATATCTATAGCGATAT	FP assay (30% GC) †
ODN 787/788*	CCATCAAAGAGAGAAAGAGC	FP assay (45% GC) ‡
ODN 786¶	CCATCAAAGATCTTTGATGG	AIM2 crystal form I
ODN 736††	CCATCAAAGAGAGAAAGAG	AIM2 crystal form II
ODN 737††	GCTCTTTCTCTCTTTGATG	AIM2 crystal form II
ODN 723††	GCCATCAAAGAGAGAG	IFI16 crystal form I
ODN 724††	TCTCTCTTTGATGGCC	IFI16 crystal form I
ODN 393‡‡	GAGAGAGA	IFI16 crystal form II
ODN 758††	CCATGACTGTAGGAAACTCTAGAGTGTA	IFI16 crystal form III
ODN 759††	GTACACTCTAGAGTTTCCTACAGTCATG	IFI16 crystal form III
dA:dT 10mer¶¶	GCATATATATGC	IL-1β stimulation assay
dA:dT 20mer¶¶	GCATATATATATATATATATGC	IL-1β stimulation assay
dA:dT 30mer¶¶	GCATATATATATATATATATATATATATATGC	IL-1β stimulation assay
dA:dT 40mer¶¶	GCATATATATATATATATATATATATATATATATATATGC	IL-1β stimulation assay
dA:dT 50mer¶¶	GCATATATATATATATATATATATATATATATATATATATATATGC	IL-1β stimulation assay
dA:dT 80mer¶¶	GCATATATATATATATATATATATATATATATATATATATATATATATATATATATATATATATATATGC	IL-1β stimulation assay
Peptides		
KS-30	KSKEKIGKEFKRIVQRIKDFLRNLVPRTES	
Scrambled KS-30	FERKEFIIVNSKPKDGQKLSVRKRTERKIL	

*These DNA oligos were labeled with 5'-Fluorescein (FAM) at the sense strand by IDT (Coralville, IA) and annealed to its reverse complement strand to form blunt-ended dsDNA.

†This oligo sequence was derived from the genomic sequence of *Francisella tularensis*.

‡This oligo sequence was derived from the genomic sequence of vaccinia virus.

¶ODN786 possesses a palindromic sequence and was annealed to itself.

††The antisense strand is listed below the sense strand (bold), and the annealed dsDNA contains 5' overhang.

‡‡ODN393 was used as a ssDNA in the IFI16 crystal form II.

¶¶These represent double stranded dA:dT oligos with 10-80mer AT sequences flanked by GC sequences at the 5' and 3'.

Table S2. X-ray Diffraction Data Collection and Refinement

	AIM2 (I)	AIM2 (II)	IFI16 (I)	IFI16 (II)[¶¶]	IFI16 m6 (III)[††]
Data Collection					
Spacegroup	$P2_1$	$P2_1$	R3	R32	R32
Unit cell (a, b, c) (Å)	58.6, 74.8, 65.5	62.4, 136.4, 77.0	126.8, 126.8, 163.9	128.6, 128.6, 67.7	128.7, 128.7, 67.8
(a, b, γ) (°)	90, 89.7, 90	90, 89.97, 90	90, 90, 120	90, 90, 120	90, 90, 120
Wavelength (Å)	1.0332	1.0332	1.0332	1.0332	1.0332
Resolution (Å) (Last shell)	50-2.55 (2.59-2.55)	50-2.50 (2.59-2.50)	50-2.50 (2.54-2.50)	50-1.80 (1.83-1.80)	50-2.25 (2.29-2.25)
No of reflections (total/unique)	77347/18538	196091/44323	187138/33125	143041/20096	101281/10296
Completeness (%)	99.8 (99.8)*	99.6 (100.0)*	97.6 (84.1)*	98.1 (85.5)*	99.7 (96.7)*
I/σ(I) (last shell)	25.5 (3.1)*	19.3 (3.3)*	21.7 (2.6)*	19.2 (2.1)*	23.5 (2.8)*
Rmerge (last shell) (%)[¶]	5.0 (61.7)*	5.3 (62.1)*	7.8 (50.5)*	8.6 (53.3)*	9.7 (59.9)*
Redundancy	4.1 (4.2)*	4.4 (4.5)*	5.6 (4.0)*	7.1 (4.6)*	9.8 (7.4)*
Rpim (last shell) (%)[§]	2.8 (34.5)*	2.9 (33.2)*	3.6 (29.2)*	3.5 (28.1)*	3.3 (23.7)*
Refinement					
Number of protein atoms	3095	6199	6309	1563	1501
No. of DNA base pairs	20 (ODN 786)	19x2 (ODN 736/737)	16 (ODN 723/724)	N/A	N/A
No. of solvent/hetero-atoms	69	199	128	211	86
Rmsd bond lengths (Å)	0.005	0.008	0.006	0.007	0.007
Rmsd bond angles (°)	0.54	0.97	0.93	1.21	1.13
Rwork (%)[†]	20.8	20.1	17.6	16.7	17.8
Rfree (%)[‡]	25.3	24.1	21.6	19.2	22.8
Ramachandran plot favored/disallowed**	94.5/0.0	94.4/0	96.1/0	98.0/0	97.9/0.0
PDB code	3RN2	3RN5	3RNU	3RLO	3RLN

*Asterisked numbers correspond to the last resolution shell.

[¶] $R_{merge} = \Sigma_h \Sigma_i |I_i(h) - \langle I(h) \rangle| / \Sigma_h \Sigma_i I_i(h)$, where $I_i(h)$ and $\langle I(h) \rangle$ are the ith and mean measurement of the intensity of reflection *h*.

[§] $R_{pim} = \Sigma_h [(1/n-1)^{1/2}] \Sigma_i |I_i(h) - \langle I(h) \rangle| / \Sigma_h \Sigma_i I_i(h)$, where $I_i(h)$ and $\langle I(h) \rangle$ are the ith and mean measurement of the intensity of reflection *h*, and n is the number of observation (redundancy) of reflection *h*.

[†] $R_{work} = \Sigma_h ||F_{obs}(h)| - |F_{calc}(h)|| / \Sigma_h |F_{obs}(h)|$, where $F_{obs}(h)$ and $F_{calc}(h)$ are the observed and calculated structure factors, respectively. No I/σ cutoff was applied.

[‡] R_{free} is the R value obtained for a test set of reflections consisting of a randomly selected 5% subset of the data set excluded from refinement.

**Values are from Molprobity server (http://molprobity.biochem.duke.edu/).

[¶¶]An 8-mer ssDNA ODN 393 (Table S1) was used to crystallize the IFI16 HINb wild type but no electron density was visible for the ssDNA.

[††]An 28-mer dsDNA ODN 758/759 (Table S1) was used to crystallize the IFI16 HINb containing K663A and R667A mutations, but no electron density was visible for the dsDNA.

Table S3. List of Residues at The HIN:DNA Interface for Each of The HIN Domains in The Three Crystal Lattices (3.5 Å Distance Cut-off)

OB1	Linker	OB2
AIM2 crystal form I*		
A160K, A162K, A163K, A198K, A204K	A244R, A251K	A267L, A287N, A309K, A311R, A335K, A337I, A340K
B160K, B162K, B163K, B198K, B204K	B247G, B248E, B249T	B287N, B309K, B311R, B335R, B337I
AIM2 crystal form II*		
A162K, A163K, A198K, A204K	A247G, A248E, A249T	A309K, A311R, A335K, A337I, A340K
B162K, B163K, B198K, B204K	B247G, B248E, B249T	B309K, B311R, B335K, B337I, B340K
C162K, C163K, C198K, C204K	C247G, C249T	C311R, C335K, C337I
D162K, D163K, D198K, D204K	D249T, D251K	D309K, D311R, D335K, D337I
IFI16 crystal form I*		
	A663K, A667R	A732K, A734K, A764R
B627K	B663K, B667R, B674K	B711T, B732K, B734K, B764R
	C663K, C667R, C674K	
	D663K, D670S	D764R

*****Each residue is denoted with a chain ID (A, B, C or D), followed by the residue number and the residue name. Each chain ID denotes a unique HIN domain in the crystal lattices.

Table S4. Mutations at the HIN domains or Full-length Proteins and Their Apparent Affinities for dsDNA Derived from The Fluorescence Polarization Assays

AIM2 HIN (mutation region)	**Mutation sites**	**Apparent Kd (μM)**
WT	-	0.034 ± 0.007
m1 (OB1)	K160A	0.060 ± 0.012
m2 (OB1)	K198A	0.035 ± 0.008
m3 (OB1)	K204A	0.065 ± 0.007
m4 (Linker)	R244A	0.070 ± 0.017
m5 (Linker)	K251A	0.090 ± 0.015
m6 (OB2)	K309A	0.084 ± 0.014
m7 (OB2)	R311A	0.038 ± 0.008
m8 (OB2)	K335A	0.049 ± 0.010
m9 (Linker)	R244A, K251A	0.139 ± 0.013
m10 (OB1)	K160A, K162A, K163A, K198A, K204A	0.139 ± 0.018
m11 (OB1 and linker)	K160A, K162A, K163A, K198A, K204A, R244A, K251A	0.168 ± 0.020
m12 (OB1, linker, and OB2)	K160A, K162A, K163A, K198A, K204A, R244A, K251A, K309A, R311A, K335A, I337A	0.223 ± 0.034
m13	F165A	0.169 ± 0.026
m0 (Irrelevant control)	K276A, K277A, K278A	0.034 ± 0.006
AIM2 FL (mutations at HIN*)	**Mutation sites***	**Apparent Kd (μM)**
WT	-	0.112 ± 0.011
m5 (Linker)	K251A	0.113 ± 0.009
m10 (OB1)	K160A, K162A, K163A, K198A, K204A	0.195 ± 0.035
m12 (OB1, linker, and OB2)	K160A, K162A, K163A, K198A, K204A, R244A, K251A, K309A, R311A, K335A, I337A	0.291 ± 0.098
m0 (Irrelevant control)	K276A, K277A, K278A	0.100 ± 0.019
IFI16 HINb (mutation region)	**Mutation sites**	**Apparent Kd (μM)**
WT	-	0.551 ± 0.075
m1 (Linker)	K663A, R667A, S670A, K674A	0.702 ± 0.068
m2 (OB1)	K627A	1.4 ± 0.18

m3 (OB2)	K732A, K734A, K759A	24 ± 2.4
m4 (OB1, linker and OB2)	K627A, K663A, R667A, S670A, K674A, K732A, K734A, K759A	32 ± 2.5
m5 (OB1 and OB2)	K627A, K732A, K734A, K759A	28 ± 1.0
m0 (Irrelevant control)	K594A, K597A, K598A, R638A, R699A	0.606 ± 0.147

* The mutation sites for the m0, m5, m10 and m12 AIM2 FL mutants are the same as the corresponding AIM2 HIN domain mutants.

Supplemental Figure Legends

Figure S1. Overview of the HIN:DNA Structures (related to Figure 2)

(A) Electron densities for the AIM2 HIN crystal form I are shown with the omit *F*o-*F*c map contoured at 3 sigma in green, and the 2*F*o-*F*c map calculated with the HIN:DNA complex contoured at 1 sigma in slate blue. The view is the same as in Figure 2A. The 5' and 3' of the dsDNA and the amino-termini of the HIN domains are marked.

(B) Electron densities for the IFI16 HINb crystal form I are shown with the omit *Fo-Fc* map contoured at 3 sigma in green, and the 2*F*o-*F*c map calculated with the HIN:DNA complex contoured at 1 sigma in slate blue. The view is the same as in Figure 2B except that two of the HINb domains are omitted for clarity.

(C) Electrostatic surface for the AIM2 HIN crystal form I is displayed on a scale of -10 kT/e (red) to 10 kT/e (blue). The bound dsDNA is shown in orange. Only one AIM2 HIN domain is presented for clarity.

(D) Electrostatic surface for the IFI16 HINb crystal form I is shown similar to that in (C). Two HINb domains are omitted for clarity. The approximate boundary between the two IFI16 HINb domains is marked with a gray dotted line.

(E) The DNA binding residues for the AIM2 HIN domain are marked on the protein surface with the residues from OB1, linker and OB2 colored yellow, magenta, and green, respectively. The view is the same as in (C).

(F) The DNA binding residues for the IFI16 HINb domains are displayed on the protein surface with the residues from OB1, linker and OB2 colored yellow, magenta, and green, respectively. The approximate boundary between the two

IFI16 HINb domains is marked with a black dotted line. The view is the same as in (D).

Figure S2. Details of The HIN:DNA Interfaces (related to Figure 3)

(A) The HIN:DNA interactions for the AIM2 HIN crystal form I is shown with the DNA-binding residues colored lime and cyan for the two HIN domains, respectively. Water molecules are in black. Hydrogen bonds involving main chains or side chains of the HIN domains are indicated as solid or dotted blue lines, respectively. Van der Waals interactions are indicated as orange lines.

(B) The HIN:DNA interactions for the AIM2 HIN crystal form II is shown similar to (A), with residues from the four HIN domains colored lime, cyan, lightpink, and wheat, respectively.

(C) The HIN:DNA interactions for the IFI16 HINb crystal form I is shown similar to (A), with residues from the four HIN domains colored lime, cyan, lightpink, and wheat, respectively.

(D) Superposition of the AIM2 HIN domain (lime) and IFI16 HINb domain (orange) with their bound dsDNA. The secondary structures are labeled for the OB1 and OB2 folds and the bound DNA molecules are colored the same as the respective HIN domains.

(E) Superposition of three representative AIM2 HIN domains from two different crystal forms in lime, cyan and lightpink, respectively, with their bound dsDNA.

(F) Superposition of four representative IFI16 HINb domains from the crystal form I lattice in lime, cyan, lightpink, and wheat, respectively, with their bound dsDNA. (G) Structure of the IFI16 HINb:DNA complex from crystal form I (lime), crystal form II (gray), and crystal form III (yellow) are superimposed with the HINb structure previously reported (PDB code 3B6Y) in magenta. The crystal forms II and III have no bound DNA visible in the electron density maps.

Figure S3. The Wild Type and Mutant AIM2 HIN Domains Bind DNA with Different Affinities (related to Figure 4)

(A) Panels for the fluorescence polarization assays of the wild type and mutant AIM2 HIN domains (m0 to m13) are displayed. The wild type binding curve is included for each mutant panel as a comparison. Details on the mutants and the affinities are in Table S4.

(B) The AIM2 residue F165 (labeled and highlighted in yellow) is located at the OB1:OB2 interface. It anchors the OB1 DNA-binding residues K160, K162, and K163 from the β1-β1' strands (marked in purple) and K198. Hydrogen bonds are illustrated as gray dotted lines and the two DNA strands are colored yellow and silver, respectively.

(C) Panels for the fluorescence polarization assays of the wild type and mutant AIM2 full-length proteins (m0, m5, m10 and m12) are displayed. The mutation sites are the same as the corresponding HIN domain mutants in (A). The wild

type binding curve is included for each mutant panel as a comparison. Details on the mutants and the affinities are in Table S4.

(D) Panels for the fluorescence polarization assays of the individual mutant IFI16 HINb domains (m0 to m5) are shown with the wild type as a comparison. Details on the mutants and the affinities are in Table S4.

Figure S4. The AIM2 PYD Domain and dsDNA Compete for HIN Domain Binding (related to Figure 6)

(A) FP assays show that DNA binding by MBP or MBP-PYD was negligible, and KS-30 peptide binds DNA with an apparent Kd of 0.17 μM.

(B) FP assays show that the AIM2 HIN domain with or without the MBP expression tag bound DNA at comparable affinities, whereas the full-length AIM2 protein had a weaker affinity for DNA.

(C) An autoinhibition model of the AIM2 receptor. AIM2 resides in an autoinhibited state in the absence of DNA binding. The PYD domain of AIM2 (electrostatic surface) forms an intramolecular complex with the HIN domain in cyan ribbons (upper left panel). Upon DNA binding, this intramolecular complex is displaced by a HIN:DNA complex (DNA in electrostatic surface), liberating the PYD domain for downstream signaling (upper right panel). The multivalent ligand DNA then facilitates the assembly of large AIM2-DNA complexes resembling the inflammasomes. The dotted line represents the linker between the AIM2 PYD and HIN domains.

Figure S5. AIM2 Oligomerizes Along The dsDNA Whereas RPA Binds ssDNA At A Different Surface of The OB Fold (related to Figure 7)

(A) Packing of the AIM2 HIN domains in the crystal form II are illustrated with the HIN domains colored cyan and marine, and the dsDNA in orange. The crystallographic asymmetric unit with four HIN domains is marked with black dotted lines.

(B) A perpendicular view of the HIN domain packing from that in (A) is shown with the same crystallographic asymmetric unit marked with black dotted lines.

(C) A hypothetical model of the AIM2 inflammasome using the HIN domain crystal lattice packing presented in (A) and (B) as a template. The dsDNA molecule at the center is represented as an orange ribbon, the protein domains are represented with their molecular surface colored cyan and marine for the AIM2 HIN domains, yellow for the AIM2 PYD domains, and orange and light magenta for the PYD and CARD domains of ASC, respectively.

(D) A perpendicular view of the AIM2 inflammasome model from that in (C). The same crystallographic asymmetric unit with four HIN domains noted in (B) is indicated again with dotted lines.

(E) The Apaf-1 apoptosome (3IZA) is represented in ribbons for comparison, with its ligand-binding domain at the peripheral and an oligomerization domain NOD (nucleotide oligomerization domain) at the center (Yuan et al., 2010). The NOD

domains are colored magenta, and the ligand-binding regulatory domains in cyan.

(F) KS-30 peptide inhibits the AIM2 HIN:DNA interaction. Increasing concentrations of the KS-30 peptide or its scrambled version were incubated with an AIM2 HIN:DNA mixture and the fluorescence polarization was analyzed with program Prism. The IC50 for the KS-30 peptide is 38 μM.

(G) The RPA SSB binds ssDNA. The OB1 and OB2 folds of the RPA SSB are colored lightpink and magenta, respectively, with the bound ssDNA as red sticks.

(H) The RPA SSB is represented as electrostatic charge surface from -10 kT/e (red) to 10 kT/e (blue), and the bound ssDNA in orange. The OB1-OB2 linker region is marked.

(I) Superposition of the AIM2 HIN with the RPA SSB using their respective OB1 modules. The view is rotated 90 degrees from that in (A). The AIM2 HIN and its bound dsDNA are shown as cyan ribbons and yellow sticks, and RPA SSB and its bound ssDNA are displayed as lightpink (OB1) /magenta (OB2) ribbons and red sticks, respectively. The gray arrow indicates a large rotation of the OB2 fold between the AIM2 HIN and RPA SSB, such that the ssDNA binding cleft in the RPA SSB is absent in the AIM2 HIN domain, and the shifted OB2 of the RPA SSB would clash with the dsDNA bound to the AIM2 HIN domain (red arrow).

Supplemental References

Adams, P.D., Afonine, P.V., Bunkoczi, G., Chen, V.B., Davis, I.W., Echols, N., Headd, J.J., Hung, L.W., Kapral, G.J., Grosse-Kunstleve, R.W.*, et al.* (2010). PHENIX: a comprehensive Python-based system for macromolecular structure solution. Acta Crystallogr D Biol Crystallogr *66*, 213-221.

Bochkarev, A., Pfuetzner, R.A., Edwards, A.M., and Frappier, L. (1997). Structure of the single-stranded-DNA-binding domain of replication protein A bound to DNA. Nature *385*, 176-181.

Chen, V.B., Arendall, W.B., 3rd, Headd, J.J., Keedy, D.A., Immormino, R.M., Kapral, G.J., Murray, L.W., Richardson, J.S., and Richardson, D.C. (2010). MolProbity: all-atom structure validation for macromolecular crystallography. Acta Crystallogr D Biol Crystallogr *66*, 12-21.

de Alba, E. (2009). Structure and interdomain dynamics of apoptosis-associated speck-like protein containing a CARD (ASC). J Biol Chem *284*, 32932-32941.

Dombrowski, Y., Peric, M., Koglin, S., Kammerbauer, C., Goss, C., Anz, D., Simanski, M., Glaser, R., Harder, J., Hornung, V.*, et al.* (2011). Cytosolic DNA triggers inflammasome activation in keratinocytes in psoriatic lesions. Sci Transl Med *3*, 82ra38.

Emsley, P., and Cowtan, K. (2004). Coot: model-building tools for molecular graphics. Acta Crystallogr D Biol Crystallogr *60*, 2126-2132.

Honig, B., and Nicholls, A. (1995). Classical electrostatics in biology and chemistry. Science *268*, 1144-1149.

Hornung, V., Ablasser, A., Charrel-Dennis, M., Bauernfeind, F., Horvath, G., Caffrey, D.R., Latz, E., and Fitzgerald, K.A. (2009). AIM2 recognizes cytosolic dsDNA and forms a caspase-1-activating inflammasome with ASC. Nature *458*, 514-518.

Hornung, V., Bauernfeind, F., Halle, A., Samstad, E.O., Kono, H., Rock, K.L., Fitzgerald, K.A., and Latz, E. (2008). Silica crystals and aluminum salts activate the NALP3 inflammasome through phagosomal destabilization. Nat Immunol *9*, 847-856.

Kabsch, W. (2010). XDS. Acta Crystallogr D Biol Crystallogr *66*, 125-132.

Kuhlman, B., Dantas, G., Ireton, G.C., Varani, G., Stoddard, B.L., and Baker, D. (2003). Design of a novel globular protein fold with atomic-level accuracy. Science *302*, 1364-1368.

Lakshiminarayanan, A.V., and Sasisekharan, V. (1970). Stereochemistry of nucleic acids and polynucleotides. II. Allowed conformations of the monomer unit for different ribose puckerings. Biochim Biophys Acta *204*, 49-59.

Laurberg, M., Asahara, H., Korostelev, A., Zhu, J., Trakhanov, S., and Noller, H.F. (2008). Structural basis for translation termination on the 70S ribosome. Nature *454*, 852-857.

Lee, B., and Richards, F.M. (1971). The interpretation of protein structures: estimation of static accessibility. J. Mol. Biol. *55*, 379-400.

Liao, J.C., Lam, R., Brazda, V., Duan, S., Ravichandran, M., Ma, J., Xiao, T., Tempel, W., Zuo, X., Wang, Y.X.*, et al.* (2011). Interferon-Inducible Protein 16: Insight into the Interaction with Tumor Suppressor p53. Structure *19*, 418-429.

Liu, L., Botos, I., Wang, Y., Leonard, J.N., Shiloach, J., Segal, D.M., and Davies, D.R. (2008). Structural basis of toll-like receptor 3 signaling with double-stranded RNA. Science *320*, 379-381.

Lu, X.J., and Olson, W.K. (2008). 3DNA: a versatile, integrated software system for the analysis, rebuilding and visualization of three-dimensional nucleic-acid structures. Nat Protoc *3*, 1213-1227.

McCoy, A.J., Grosse-Kunstleve, R.W., Adams, P.D., Winn, M.D., Storoni, L.C., and Read, R.J. (2007). Phaser crystallographic software. J Appl Crystallogr *40*, 658-674.

Painter, J., and Merritt, E.A. (2006). Optimal description of a protein structure in terms of multiple groups undergoing TLS motion. Acta Crystallogr D Biol Crystallogr *62*, 439-450.

Potterton, E., Briggs, P., Turkenburg, M., and Dodson, E. (2003). A graphical user interface to the CCP4 program suite. Acta Crystallogr D Biol Crystallogr *59*, 1131-1137.

Rai, B.K., and Fiser, A. (2006). Multiple mapping method: a novel approach to the sequence-to-structure alignment problem in comparative protein structure modeling. Proteins *63*, 644-661.

Rathinam, V.A., Jiang, Z., Waggoner, S.N., Sharma, S., Cole, L.E., Waggoner, L., Vanaja, S.K., Monks, B.G., Ganesan, S., Latz, E.*, et al.* (2010). The AIM2 inflammasome is essential for host defense against cytosolic bacteria and DNA viruses. Nat Immunol *11*, 395-402.

Ritchie, D.W., Kozakov, D., and Vajda, S. (2008). Accelerating and focusing protein-protein docking correlations using multi-dimensional rotational FFT generating functions. Bioinformatics *24*, 1865-1873.

Tokumaru, S., Sayama, K., Shirakata, Y., Komatsuzawa, H., Ouhara, K., Hanakawa, Y., Yahata, Y., Dai, X., Tohyama, M., Nagai, H.*, et al.* (2005). Induction of keratinocyte migration via transactivation of the epidermal growth factor receptor by the antimicrobial peptide LL-37. J Immunol *175*, 4662-4668.

Wang, G. (2008). Structures of human host defense cathelicidin LL-37 and its smallest antimicrobial peptide KR-12 in lipid micelles. The Journal of biological chemistry *283*, 32637-32643.

Yang, D., Chertov, O., and Oppenheim, J.J. (2001). Participation of mammalian defensins and cathelicidins in anti-microbial immunity: receptors and activities of human defensins and cathelicidin (LL-37). Journal of leukocyte biology *69*, 691-697.

Yang, H., Guranovic, V., Dutta, S., Feng, Z., Berman, H.M., and Westbrook, J.D. (2004). Automated and accurate deposition of structures solved by X-ray

diffraction to the Protein Data Bank. Acta Crystallogr D Biol Crystallogr *60*, 1833-1839.

Yuan, S., Yu, X., Topf, M., Ludtke, S.J., Wang, X., and Akey, C.W. (2010). Structure of an apoptosome-procaspase-9 CARD complex. Structure *18*, 571-583.

Zbyszek Otwinowski, W.M. (1997). Processing of X-ray Diffraction Data Collected in Oscillation Mode In Methods Enzymol (Academic Press), pp. 307-326.

Fig. S1

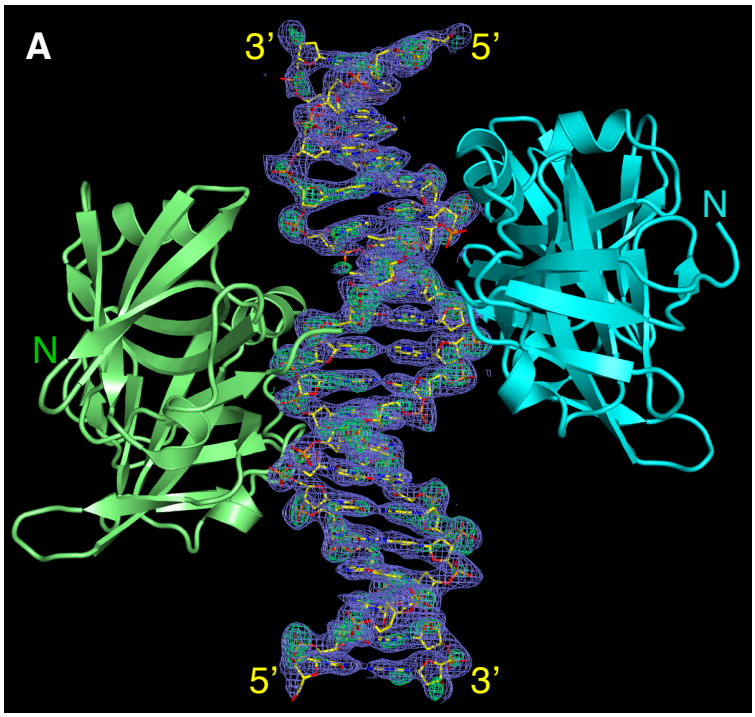

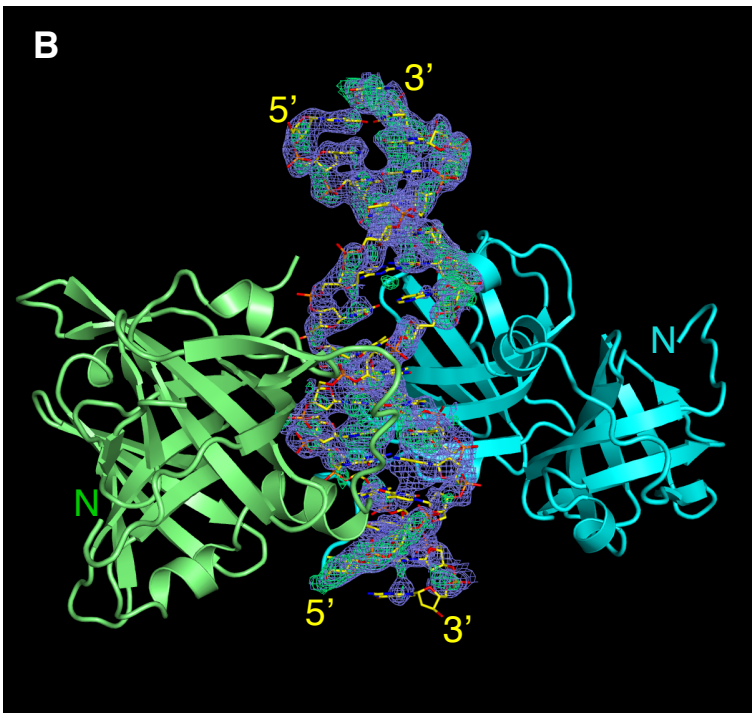

Fig. S1

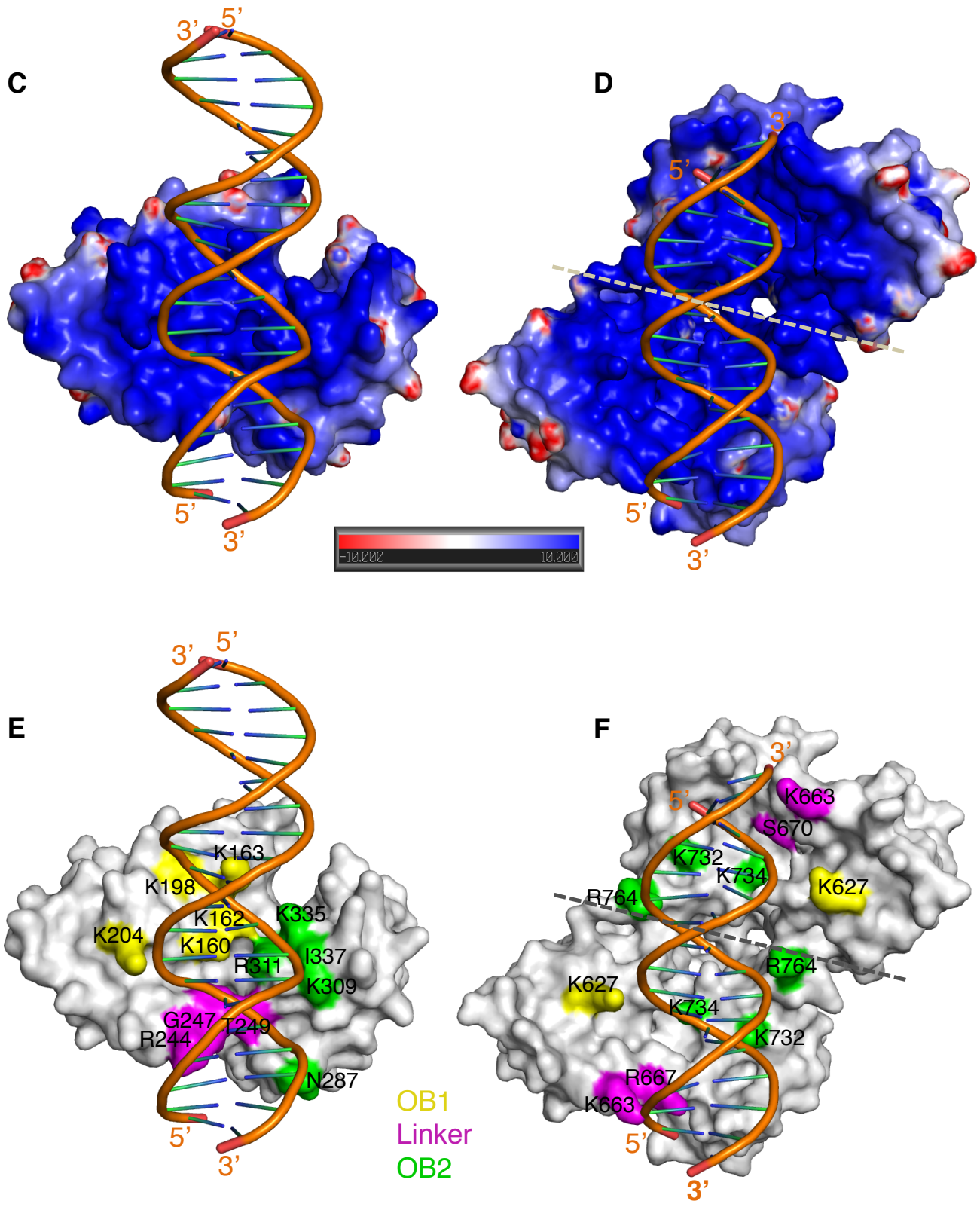
C
D
3’
5’
5’
3’
-10.000
10.000
E
F
K163
K198
K162
K335
K204
K160
R311
I337
K309
G247
T249
R244
N287
OB1
Linker
OB2
K663
S670
K732
K734
K627
R764
R667

Fig. S2

A

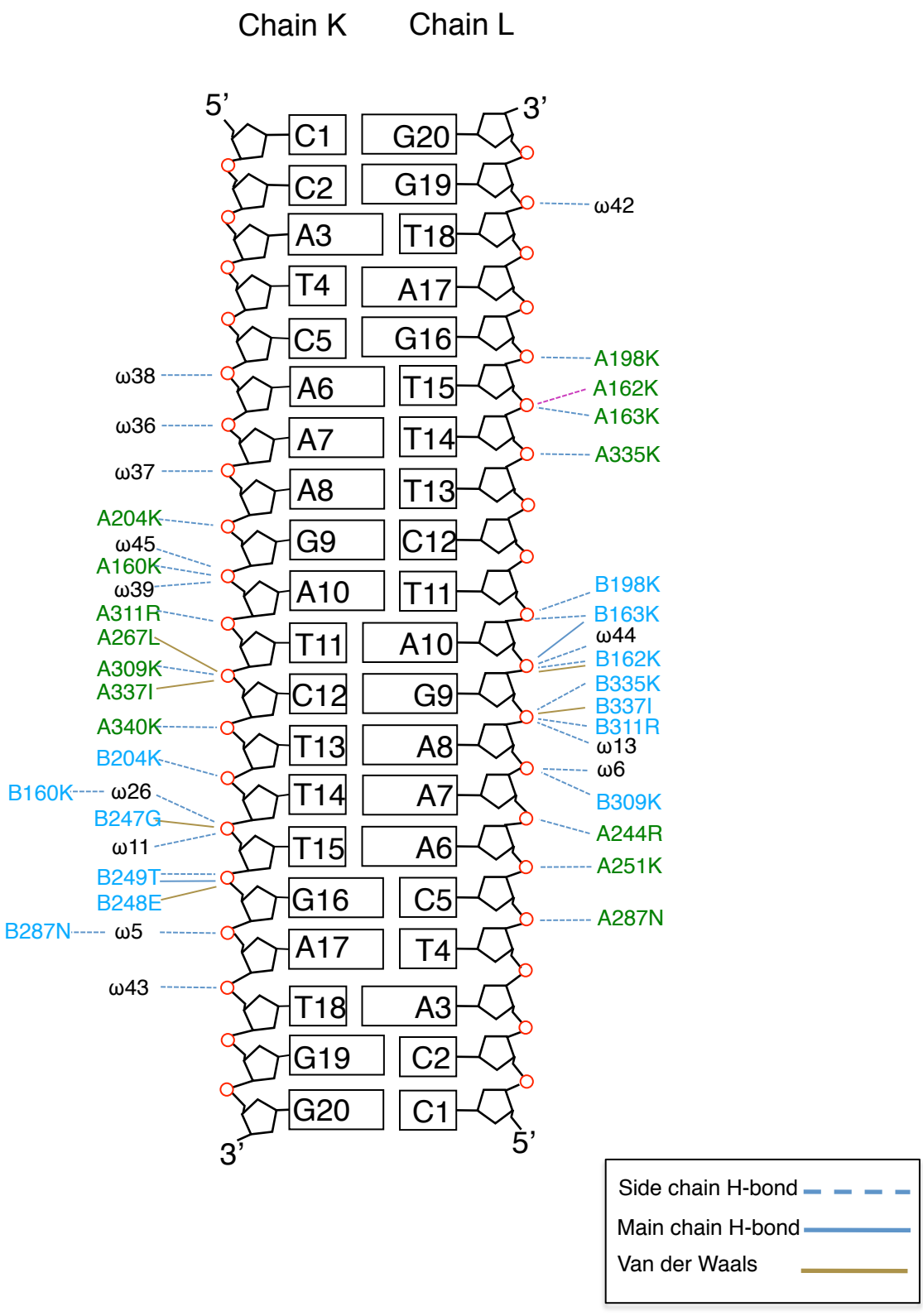
Chain K
Chain L
5’
3’
C1
G20
C2
G19
A3
T18
T4
A17
C5
G16
A6
T15
A7
T14
A8
T13
G9
C12
A10
T11
T11
A10
C12
G9
T13
A8
T14
A7
T15
A6
G16
C5
A17
T4
T18
A3
G19
C2
G20
C1
3’
5’
ω42
A198K
A162K
A163K
A335K
ω38
ω36
ω37
A204K
ω45
A160K
ω39
A311R
A267L
A309K
A337I
A340K
B204K
B160K
ω26
B247G
ω11
B249T
B248E
B287N
ω5
ω43
B198K
B163K
ω44
B162K
B335K
B337I
B311R
ω13
ω6
B309K
A244R
A251K
A287N
Side chain H-bond
Main chain H-bond
Van der Waals

Fig. S2

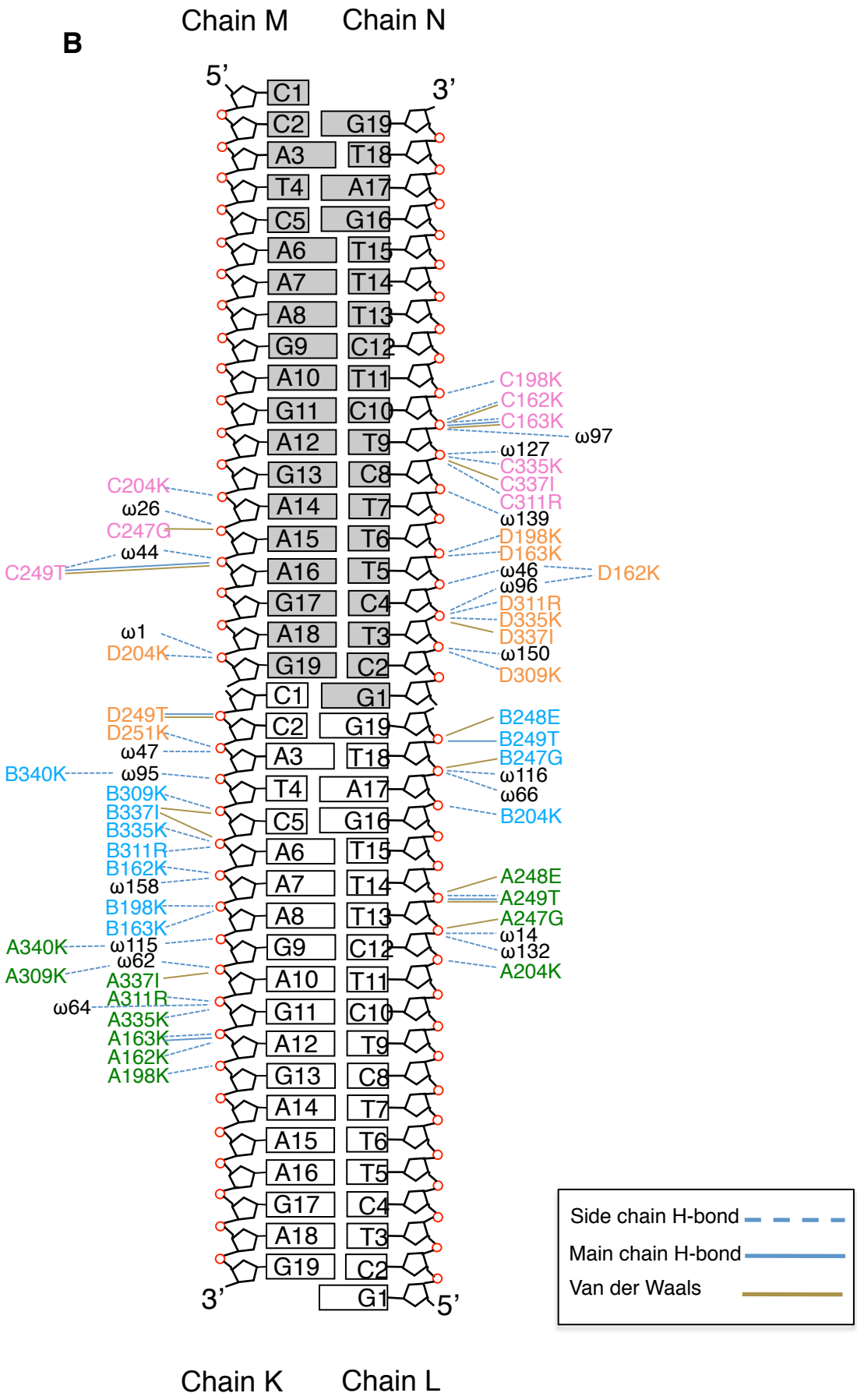
B
Chain M
Chain N
5'
3'
C1 G19
C2 T18
A3 T17
T4 G16
C5 T15
A6 T14
A7 T13
A8 C12
G9 T11
A10 C10
G11 T9
A12 C8
G13 T7
A14 T6
A15 T5
A16 C4
A17 T3
A18 C2
G19 G1
C1 G19
C2 T18
A3 T17
T4 G16
C5 T15
A6 T14
A7 T13
A8 C12
G9 T11
A10 C10
G11 T9
A12 C8
G13 T7
A14 T6
A15 T5
A16 C4
G17 T3
A18 C2
G19 G1
3'
5'
C198K
C162K
C163K
ω97
ω127
C335K
C337I
C311R
ω139
D198K
D163K
ω46
D162K
ω96
D311R
D335K
D337I
ω150
D309K
B248E
B249T
B247G
ω116
ω66
B204K
A248E
A249T
A247G
ω14
ω132
A204K
C204K
ω26
C247G
ω44
C249T
ω1
D204K
D249T
D251K
ω47
B340K
ω95
B309K
B337I
B335K
B311R
B162K
ω158
B198K
B163K
A340K
ω115
ω62
A309K
A337I
ω64
A311R
A335K
A163K
A162K
A198K
Side chain H-bond
Main chain H-bond
Van der Waals
Chain K
Chain L

Fig. S2

C

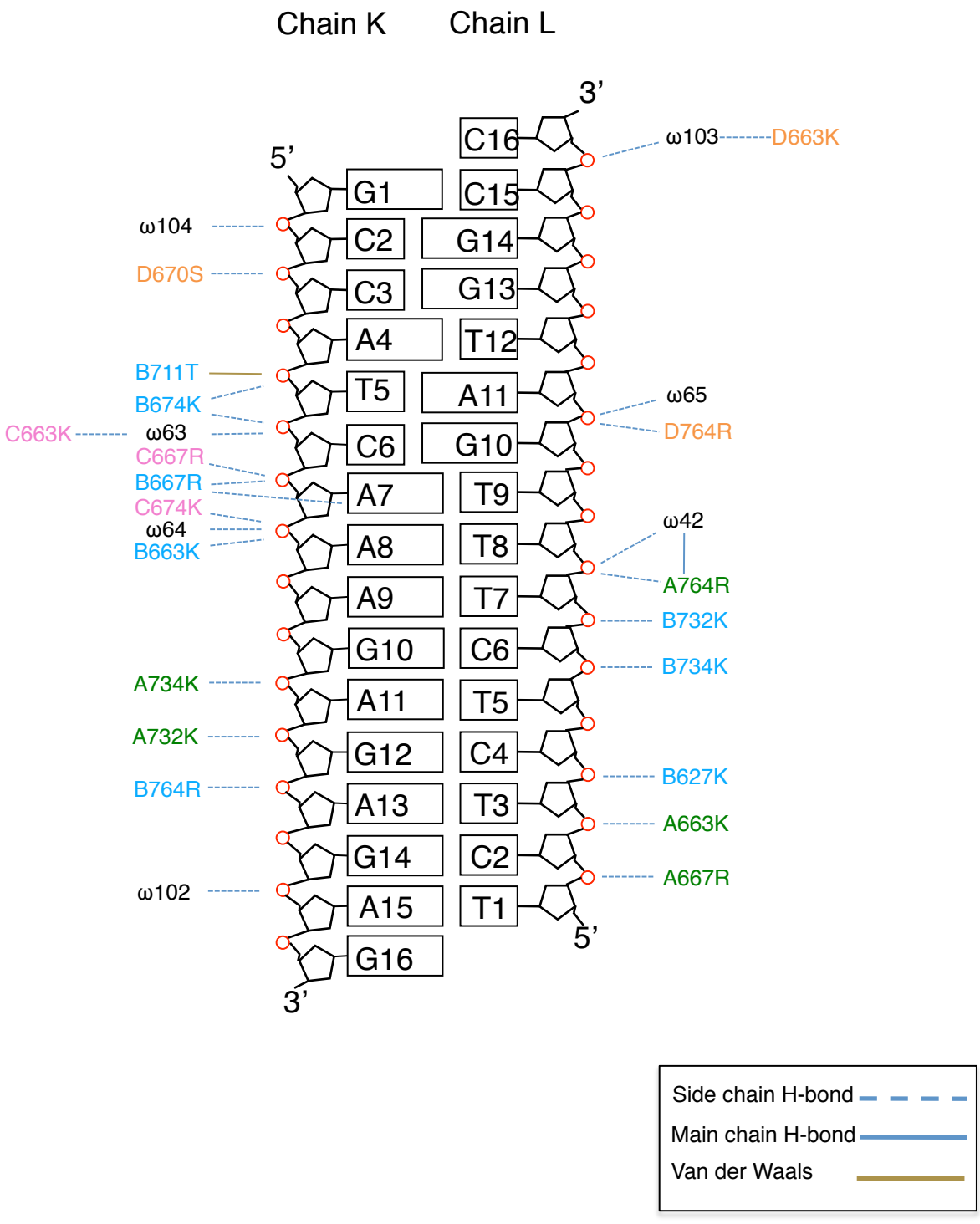
Chain K
Chain L
3'
5'
C16
G1
C15
C2
G14
C3
G13
A4
T12
T5
A11
C6
G10
A7
T9
A8
T8
A9
T7
G10
C6
A11
T5
G12
C4
A13
T3
G14
C2
A15
T1
G16
5'
3'
ω103
D663K
ω104
D670S
B711T
B674K
C663K
ω63
C667R
B667R
C674K
ω64
B663K
ω65
D764R
ω42
A764R
B732K
B734K
A734K
A732K
B764R
B627K
A663K
A667R
ω102
Side chain H-bond
Main chain H-bond
Van der Waals

Fig. S2

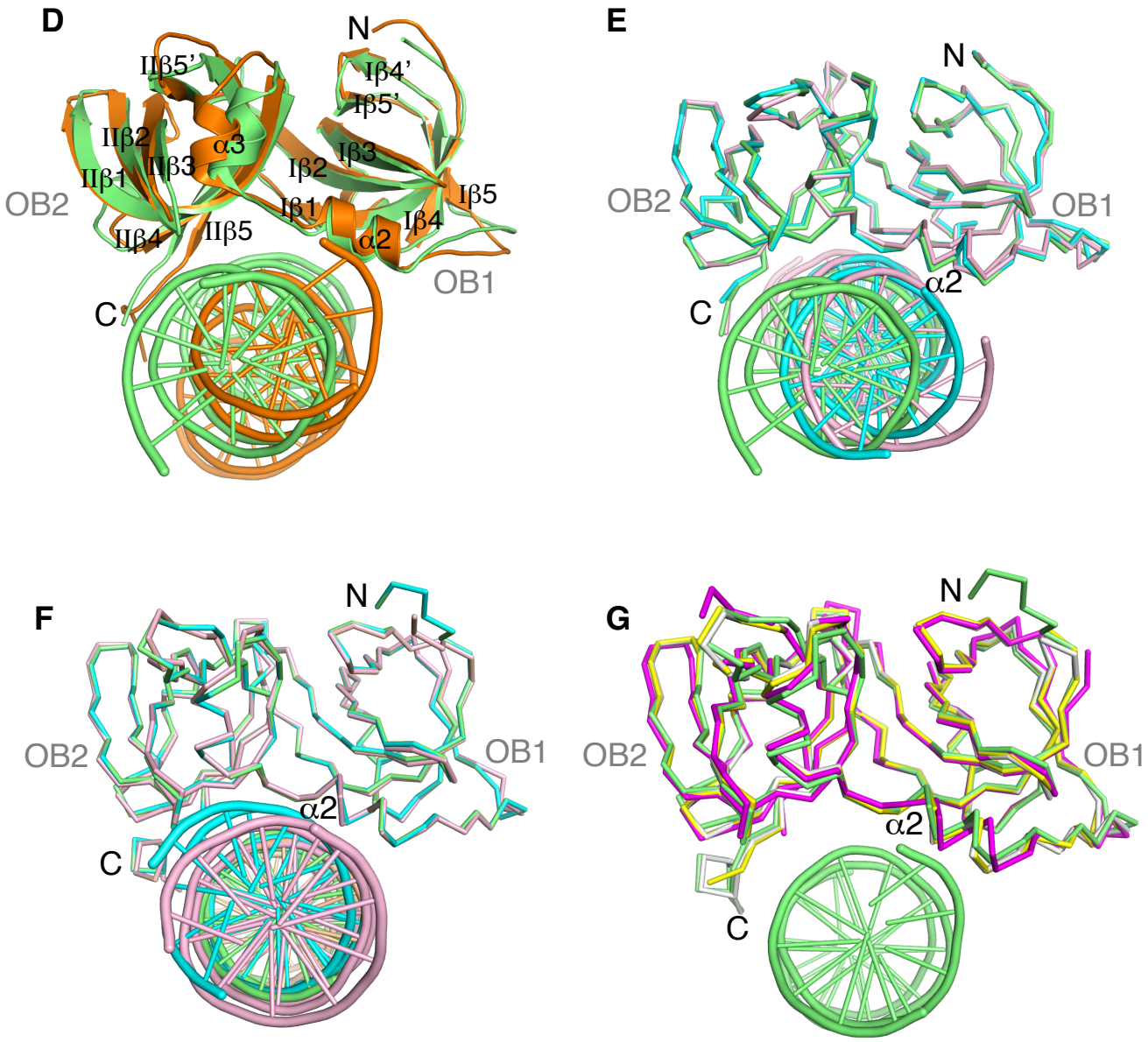
D
N
IIβ5'
Iβ4'
Iβ5'
IIβ2
α3
Iβ3
IIβ1
IIβ3
Iβ2
Iβ5
OB2
Iβ1
Iβ4
IIβ4
IIβ5
α2
OB1
C
E
N
OB2
OB1
α2
C
F
N
OB2
OB1
α2
C
G
N
OB2
OB1
α2
C

Fig. S3

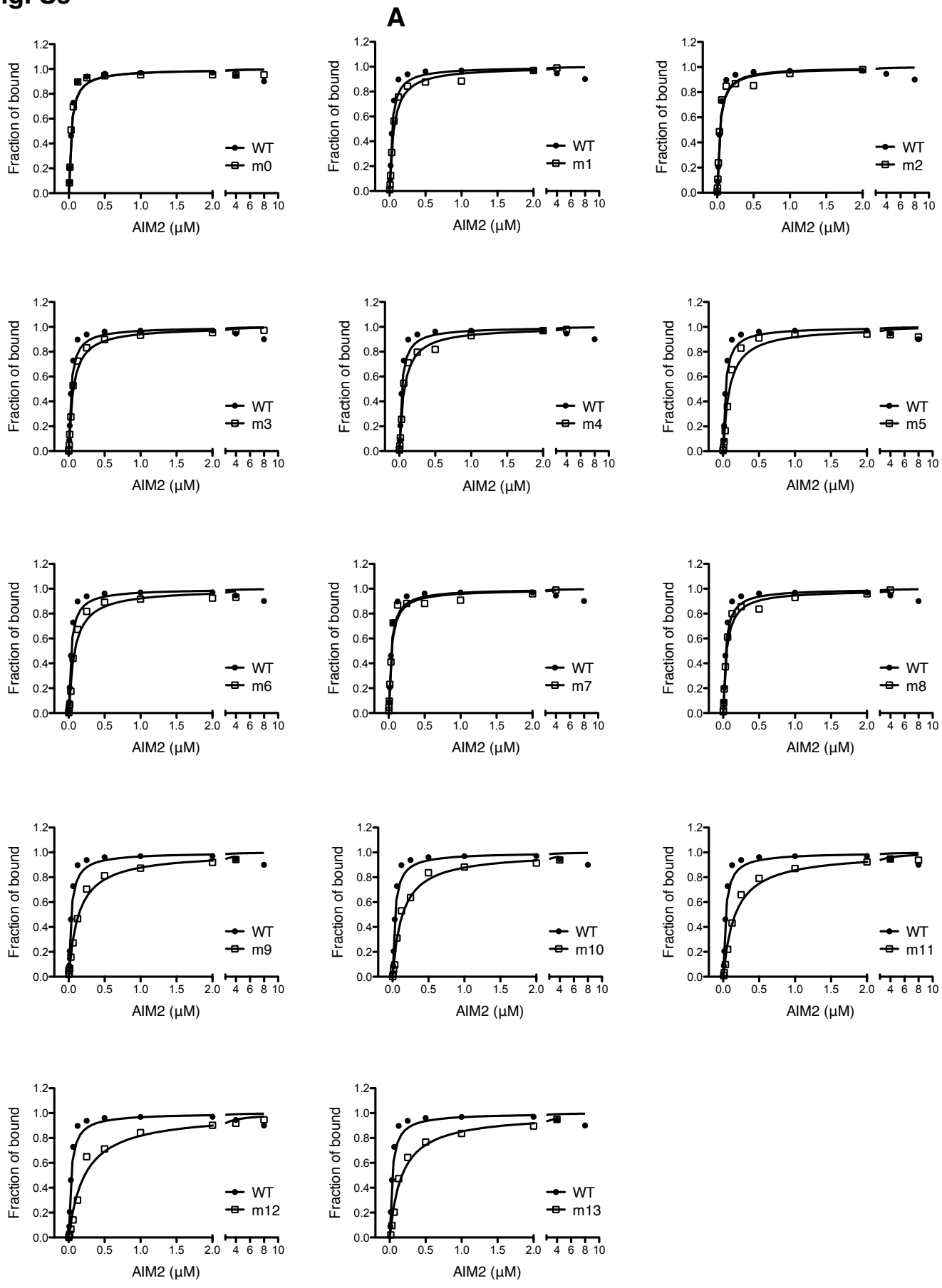
A
Fraction of bound
AIM2 (μM)
WT
m0
m1
m2
m3
m4
m5
m6
m7
m8
m9
m10
m11
m12
m13

Fig. S3

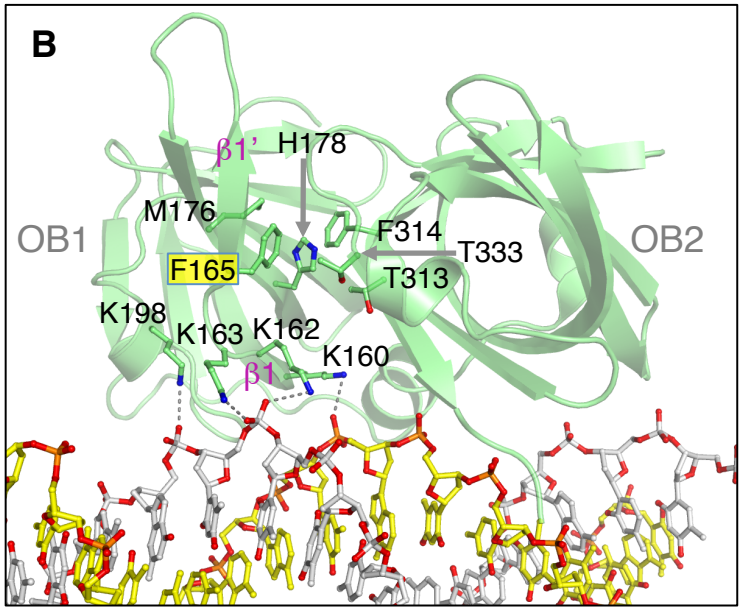
B
β1'
H178
M176
OB1
F314
T333
OB2
F165
T313
K198
K163
K162
K160
β1

C

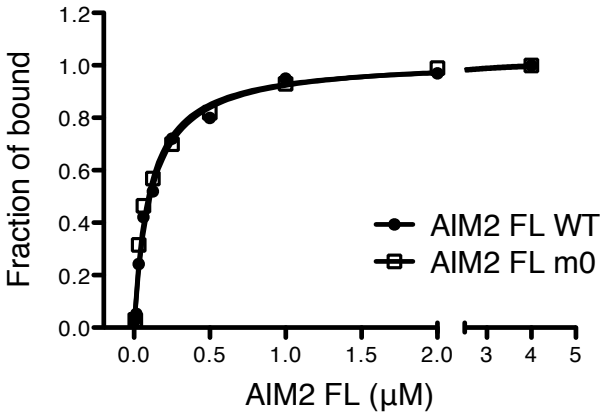
Fraction of bound
AIM2 FL WT
AIM2 FL m0
AIM2 FL (μM)

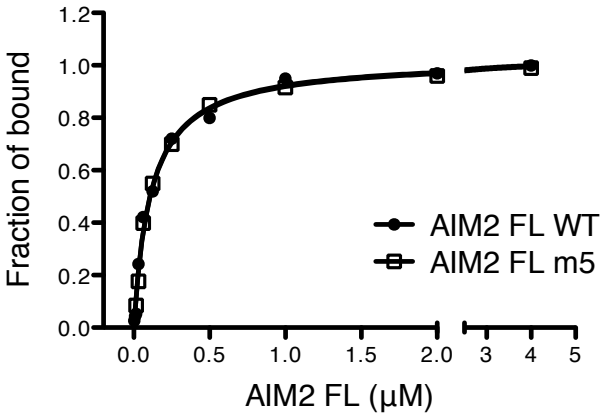
Fraction of bound
AIM2 FL WT
AIM2 FL m5
AIM2 FL (μM)

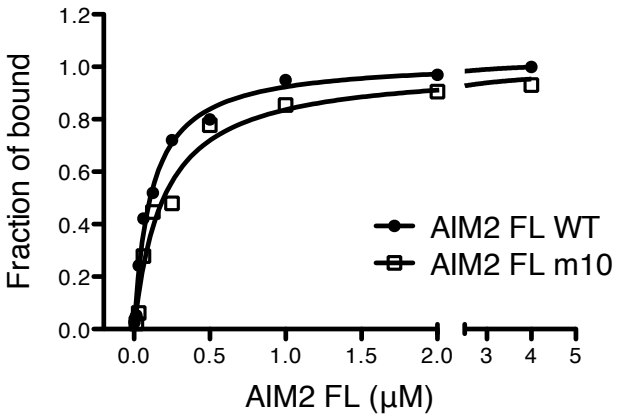
Fraction of bound
AIM2 FL WT
AIM2 FL m10
AIM2 FL (μM)

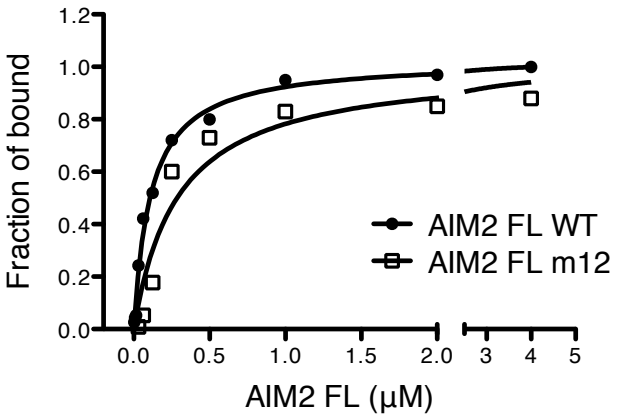
Fraction of bound
AIM2 FL WT
AIM2 FL m12
AIM2 FL (μM)

Fig. S3

D

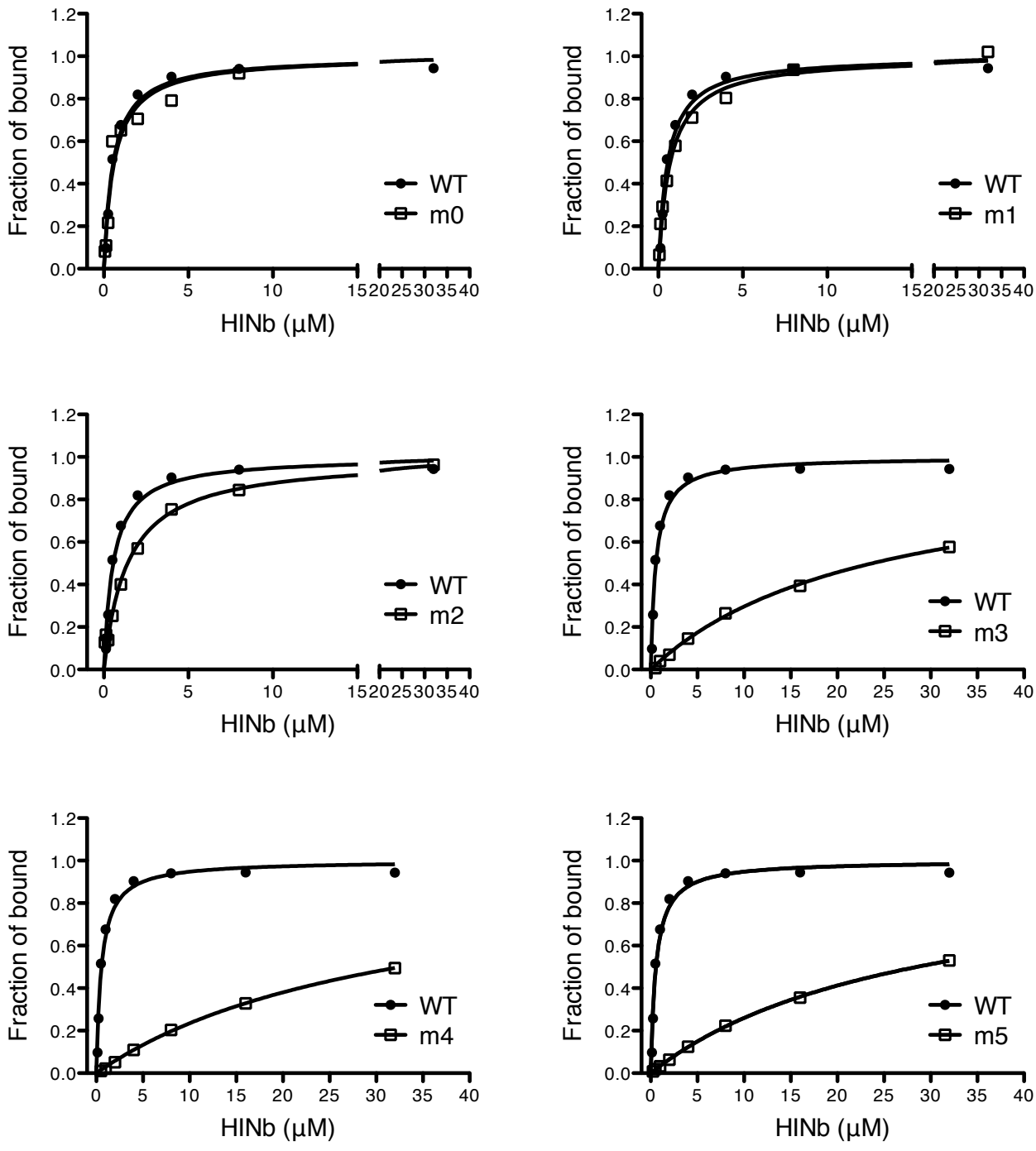

Fig. S4

A

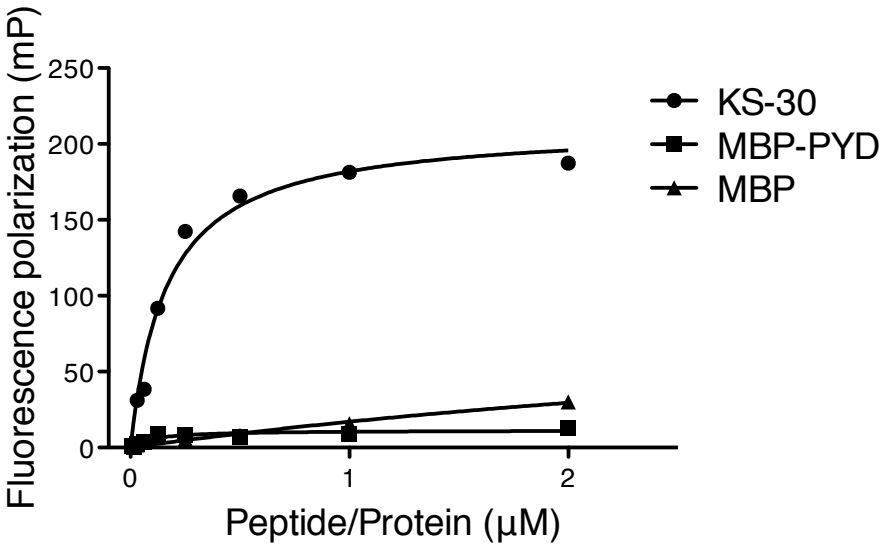

B

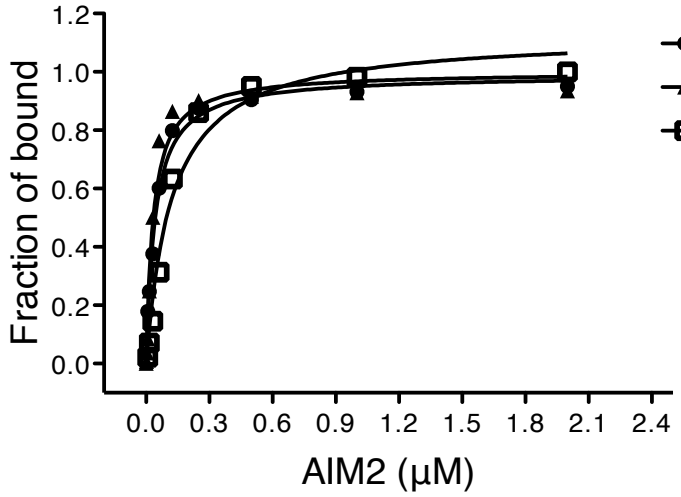

	Kd[a] (μM)
HIN	0.042±0.004
MBP-HIN	0.033±0.006
MBP-FL AIM2	0.122±0.025

C

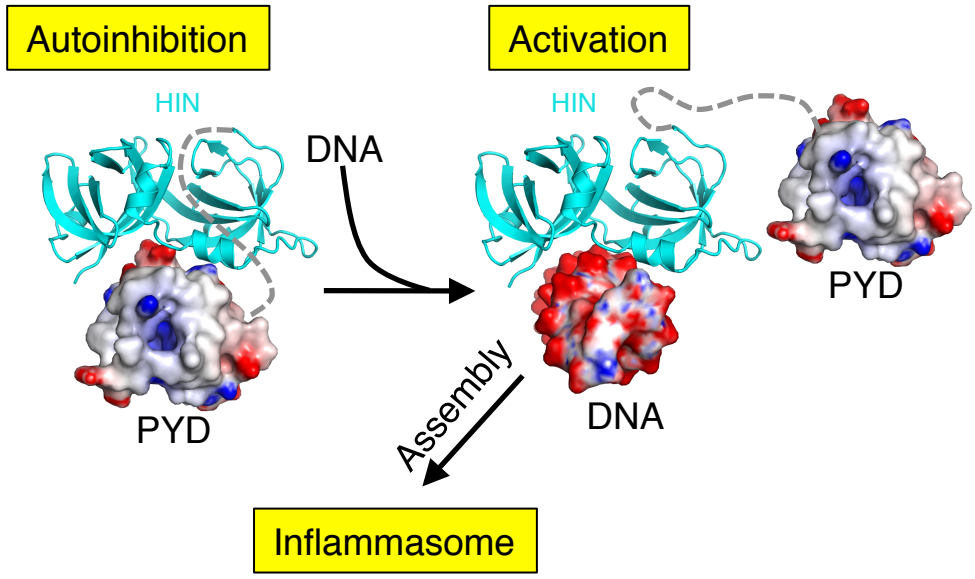

Fig. S5

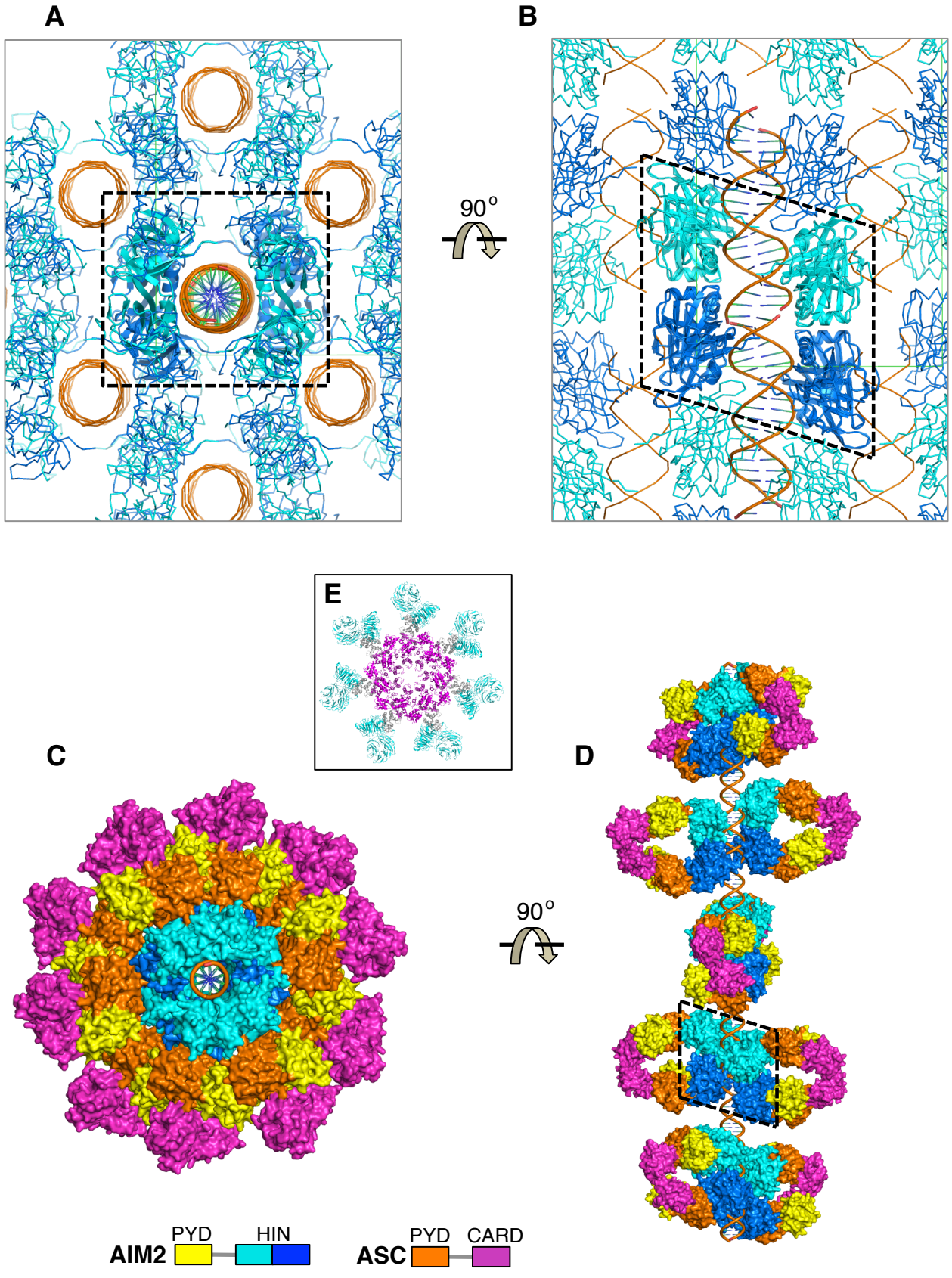

Fig. S5

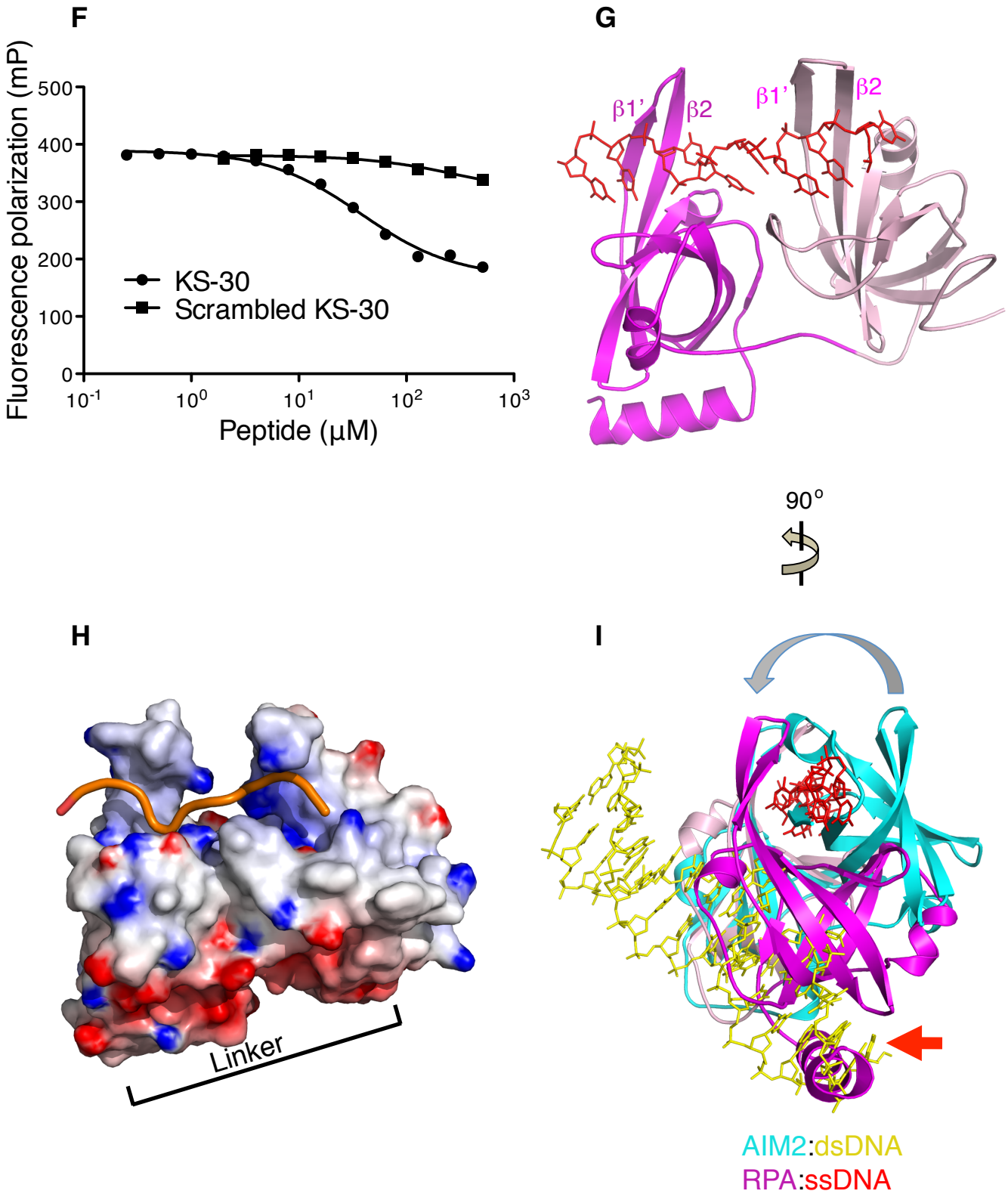
F
Fluorescence polarization (mP)
500
400
300
200
100
0
10^{-1}
10^{0}
10^{1}
10^{2}
10^{3}
Peptide (μM)
KS-30
Scrambled KS-30
G
β1'
β2
β1'
β2
90°
H
Linker
I
AIM2:dsDNA
RPA:ssDNA